Applied Physics
Express

LETTER • OPEN ACCESS

Role of hot phonons and layer geometry in spintronic terahertz emission

OPEN ACCESS
Applied Physics Express 18, 093001 (2025) LETTER
https://doi.org/10.35848/1882-0786/adfef2

Role of hot phonons and layer geometry in spintronic terahertz emission

Byungwoo Son[1], Yeongwoo Ahn[2], Hanbum Park[3], Dogeun Jang[4], Kyusup Lee[2*], Hyunsoo Yang[3*], and Do-Kyeong Ko[1*]

[1]Department of Physics and Photon Science, Gwangju Institute of Science and Technology, Gwangju 61005, Republic of Korea
[2]Department of Physics, Pukyong National University, Busan 41005, Republic of Korea
[3]Department of Electrical and Computer Engineering, National University of Singapore, 117576, Singapore
[4]Pohang Accelerator Laboratory, POSTECH, Pohang 37673, Republic of Korea

*E-mail: kslee@pknu.ac.kr; eleyang@nus.edu.sg; dkko@gist.ac.kr

Received June 19, 2025; revised July 20, 2025; accepted August 24, 2025; published online September 4, 2025

We compare terahertz (THz) emission from bilayer and trilayer spintronic structures optimized for femtosecond laser excitation. The trilayer shows approximately twice the THz amplitude of the bilayer, owing to constructive spin-to-charge conversion at both interfaces. However, saturation behavior emerges in the trilayer due to hot phonon effects. Time-domain analysis of the extracted charge currents reveals distinct ultrafast spin transport dynamics. These results highlight the role of multilayer design and phonon interactions in enhancing the performance of spintronic THz emitters.

A spin current, the flow of spin-polarized electrons, forms the basis of modern low-power information technologies. Owing to the absence of net electric current, spin currents can propagate without Joule heating. To achieve energy efficient and high-speed signal processing, both low dissipation and ultrafast response are essential, potentially enabling computing speeds up to the terahertz (THz) regime.[1)] In this context, THz spintronics—relying on picosecond spin current generation and detection—has gained significant attention.[2,3)]

Ultrashort spin currents can be induced in ferromagnetic metals (FMs) by femtosecond laser excitation via the superdiffusive transport mechanism.[4)] When excited by near-infrared pulses, high-energy photons generate non-equilibrium electrons in the FM, which move ballistically before thermalizing within ~1 ps.[5,6)] The electrons with opposite spin polarizations exhibit different mobilities, producing an ultrashort spin-polarized current inside the FM layer.

To detect these spin currents, a heavy nonmagnetic metal (NM) with strong spin–orbit coupling (e.g. Pt, W, or Ta) is placed in contact with the FM. The longitudinal spin currents ($\mathbf{J}_s$) entering the NM are converted to transverse charge currents ($\mathbf{J}_c$) typically via the inverse spin Hall effect, occurring on sub-picosecond timescales.[7)] These ultrashort $\mathbf{J}_c$ bursts act as THz radiation sources [Fig. 1(a)]. The resulting nm-thin FM/NM structures are referred to as spintronic THz emitters (STEs).[8)]

Efforts over the past decade have focused on enhancing the spin-to-charge conversion (SCC) efficiency and THz emission amplitude, including optimization of thicknesses, interface engineering, and multilayer design with different capping. Notably, trilayer structures (NM/FM/NM) have been proposed to outperform conventional bilayers (NM/FM). In a bilayer, only one FM/NM interface contributes to $\mathbf{J}_c$ generation, whereas trilayers provide two interfaces. If the two NM layers have opposite spin Hall angles (θ_{SH}), the generated J_c from both sides adds constructively, enhancing THz emission [Fig. 1(b)].

However, THz emission depends on various factors: optical absorption, film thickness, spin diffusion lengths, the substrate refractive index.[9–12)] Therefore, optimized thickness for bilayer and trilayer structures may differ, and direct comparisons under their respective optimal conditions are still elusive.

In this study, we compare the THz output from bilayer and trilayer STEs under optimized conditions. THz time-domain spectroscopy is performed using a femtosecond laser (800 nm, 70 fs, 1 kHz, and 1.5 W). The beam is split into pump and probe paths. The pump excited the STE, while the probe, delayed via a motorized stage, is used for electro-optic sampling with a 1 mm thick ZnTe crystal, enabling time-resolved detection of the emitted THz field.

As a benchmark, we first measured the THz waveform emitted from a ⟨110⟩-cut 1 mm thick ZnTe crystal [Fig. 2(a)]. For the STEs using femtosecond laser excitation, the optimal thicknesses depend on the sample geometries.[13,14)] We selected the optimal thicknesses for the THz emission based on the references: Pt (6 nm)/Co (3 nm) bilayer[13)] and W (2 nm)/Co (2 nm)/Pt (2 nm) trilayer.[14)] These thin films were deposited on both-side polished quartz substrates with a 2 inch diameter using DC magnetron sputtering at room temperature. The optical damage threshold is found to be ~1.3 mJ cm^{-2}. A custom-designed Halbach-type magnet array [Fig. 1(c)] enables a uniform in-plane magnetic field >1 kOe, ensuring the saturated FM magnetization.

Figures 2(b) and 2(c) show clear THz signal polarity reversal upon magnetic field reversal, confirming the magnetic origin. Both structures produce THz fields roughly two orders of magnitude stronger than Co-only films, underscoring the dominant role of SCC-mediated charge acceleration over magnetic dipole radiation. The trilayer emits THz signals comparable to the ZnTe crystal and about twice as strong as the bilayer at ~1 mJ cm^{-2} pump fluence. The optical-to-THz conversion efficiency of the trilayer reaches ~10^{-4} at 4 mJ pump energy. This can be further improved by multilayer coatings and buffer layers for enhanced absorption and thermal dissipation.[15)]

We next study the optical fluence dependence of the THz output [Figs. 3(a) and 3(b)]. THz amplitude increases with fluence for both STEs, with the trilayer consistently emitting nearly twice as strongly [Fig. 3(d)]. This aligns with the

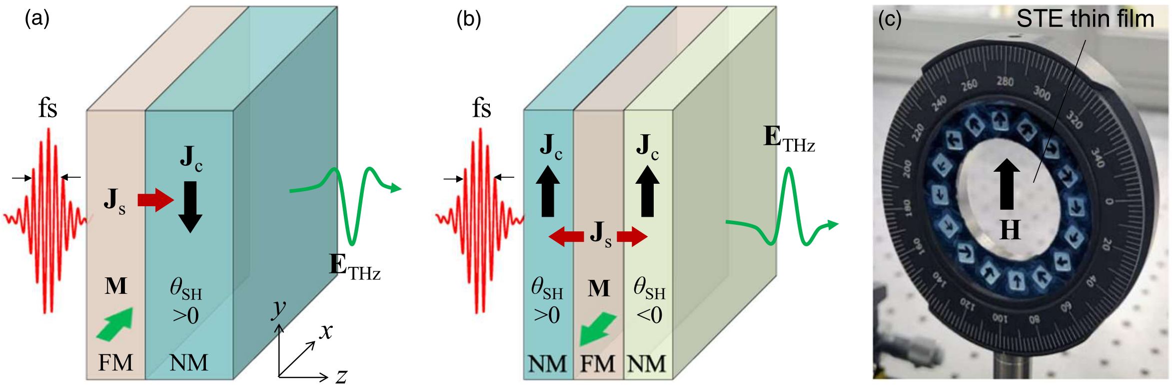

Fig. 1. Schematics of optical-driven THz emission mechanisms based on (a) bilayer and (b) trilayer structures. (c) The STE sample mounted in a 2 inch rotational holder with a custom-designed Halbach-type magnet array.

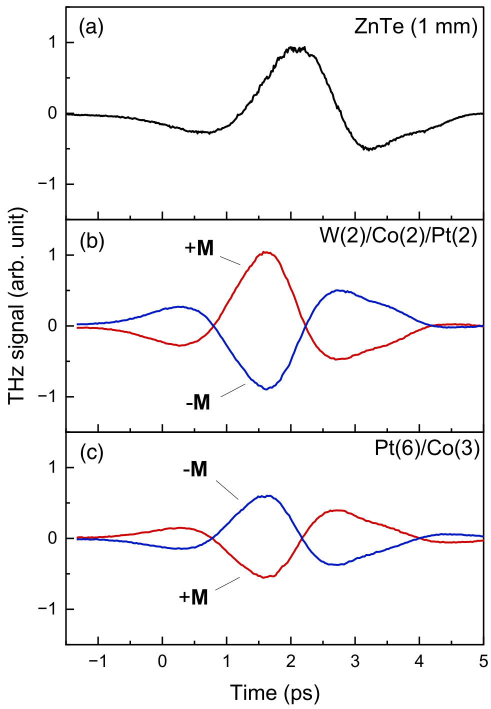

Fig. 2. THz signals emitted from (a) a 1 mm thick ZnTe crystal, (b) the W (2 nm)/Co (2 nm)/Pt (2 nm) trilayer, and (c) the Pt (6 nm)/Co (3 nm) bilayer.

expectation that the in-phase $\mathbf{J}_c$ from both NM layers in the trilayer leads to stronger emission.

Importantly, we observe comparable THz amplitudes under collimated and diverging beam conditions [Fig. 3(c)], reflecting the dipole nature of the emission. This angular insensitivity enables simple and compact optical setups, favorable for portable THz sources.[16]

Interestingly, the trilayer signal saturates beyond $\sim$0.8 mJ cm^{-2}, while the bilayer response remains linear. This saturation likely originates from the hot-phonon bottleneck effect.[17] The optically excited electrons (hot carriers) transfer their energy to phonons and quickly relax, elevating the effective phonon temperature and generating hot phonons. During this thermalization, these hot phonons are simultaneously reabsorbed by the hot carriers, making the cooling process inefficient under stronger optical excitation and with the increased number of hot carriers. Since the spin current $\mathbf{J}_s$ depends on spin transfer over the relaxation timescale, the phonon bottleneck effect reduces the spin current magnitude, thereby leading to the observed saturation of the emitted THz radiation.

To further probe ultrafast spin dynamics from the measured THz signal $S(\omega) = R(\omega) \times E_{THz}(\omega)$, we extract $\mathbf{J}_c$ directly using the relation $J_c(\omega) = \sigma(\omega) \times E_{THz}(\omega)$. Here $R(\omega)$ is the detector response function, and $\sigma(\omega)$ is the sheet conductivity derived from the THz time-domain spectroscopy with thin-film approximation:[8,18,19]

$$\sigma(\omega) = \frac{(n+1)}{Z_0 d}\left(\frac{E_{ref}(\omega)}{E_{sam}(\omega)} - 1\right), \quad (1)$$

where n is the refractive index, Z_0 is the impedance of free space, d is the film thickness, and $E_{ref}(\omega)$ and $E_{sam}(\omega)$ are the reference and sample transmitted THz fields, respectively.

Figures 4(a) and 4(b) show the extracted $\mathbf{J}_c$ waveforms at various fluences. Similar to the THz amplitude trends (Fig. 3), the trilayer exhibits saturation at high fluence, while the bilayer does not [Fig. 4(c)].

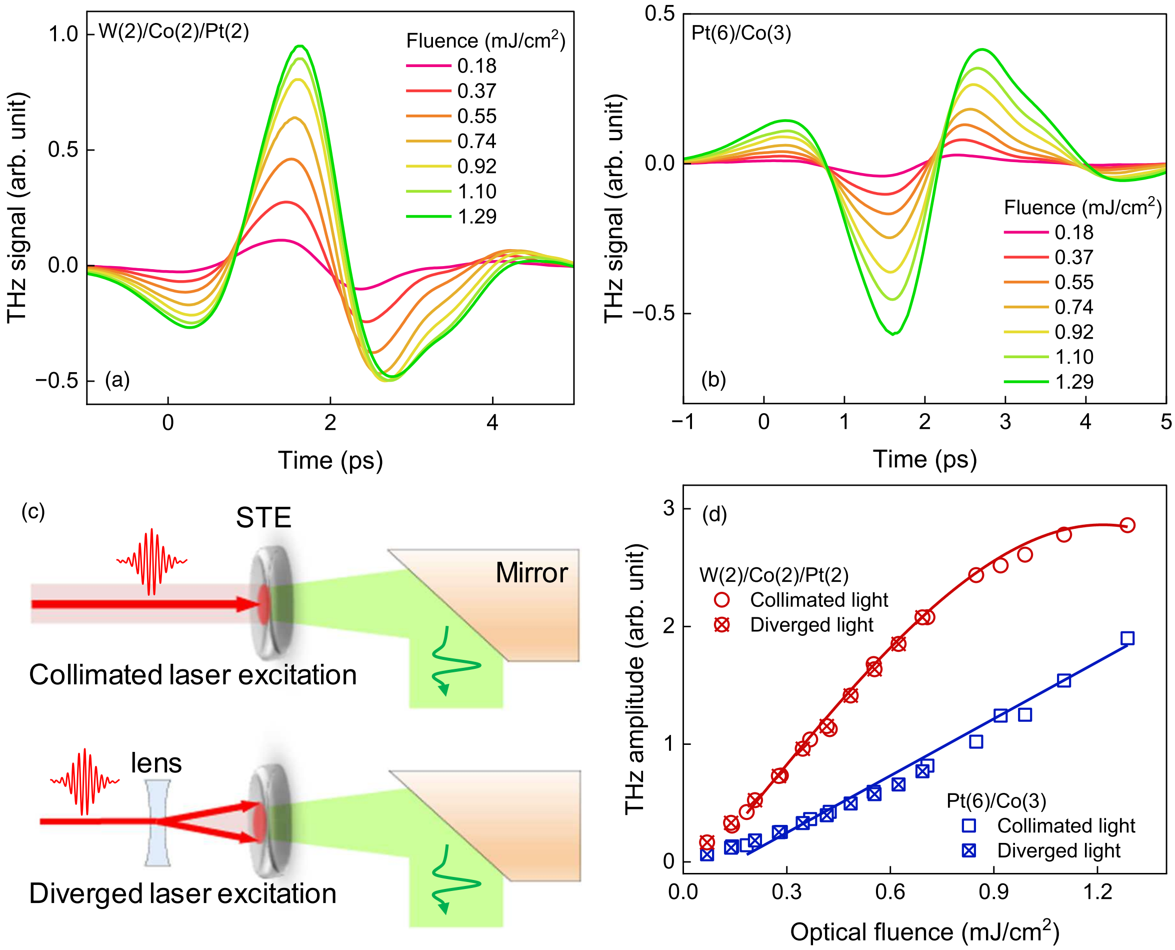

Fig. 3. THz signals measured at different optical fluences for (a) the trilayer, and (b) the bilayer. (c) Schematic diagram of the THz emission setup with collimated and diverged laser excitation. (d) Peak-to-peak amplitude of the THz signals versus optical fluence for both STEs. The THz amplitudes are also compared depending on the two laser excitation schemes. The numbers in parentheses indicate the thickness in nm.

Temporal analysis of $\mathbf{J}_c$ peaks reveals distinct trends [Fig. 4(d)]. For the bilayer, the peak delays and saturates beyond $\sim$0.8 mJ cm^{-2}. For the trilayer, the $\mathbf{J}_c$ peak is initially delayed and then advances beyond a critical fluence near 0.55 mJ cm^{-2}. These distinct nonlinear behaviors can be attributed to the role of hot phonons in modulating spin relaxation dynamics. As the pump fluence increases, the phonons bottleneck effect prolongs the spin relaxation time, delaying the timing and reducing the magnitude of both $\mathbf{J}_s$ and $\mathbf{J}_c$. For the bilayer, the absence of a critical fluence and the monotonic saturation of the $\mathbf{J}_c$ peak suggest a dominant collision-limited regime, where the hot phonon accumulation gradually suppresses the ultrafast spin transport. On the other hand, for the trilayer, the presence of a critical fluence corresponds to a transition from a collision-limited regime at lower fluences to a collision-free ballistic transport regime at higher fluences. This transition is governed by the interplay between phonon scattering and spin transport pathways, which are strongly influenced by the multilayer geometry, materials, and interface quality.[20] Therefore, the peak shift and saturation behaviors observed in Fig. 4(d) can be attributed to phonon dynamics coupled with the structural differences between the bilayer and trilayer, which dictate their respective spin relaxation and transport regimes. In particular, compared to Pt, the presence of W in the trilayer enhances phonon-mediated scattering, resulting in stronger delay modulation.[21] In this regard, while W is a good candidate for the trilayer STE because it exhibits the most efficient spin-to-charge conversion among typical heavy elements with a negative spin Hall angle,[13,14] it would be beneficial to further investigate other elements with a larger negative spin Hall angle, particularly for achieving high-power THz emission.

In conclusion, we systematically compare bilayer and trilayer spintronic THz emitters under optimized conditions and find that trilayers exhibit approximately twice the THz output. However, saturation due to hot phonon effects appears in trilayers, while bilayers maintain linearity. Extraction of ultrafast charge currents reveals unique spin transport dynamics in each case. Our results underscore the importance of multilayer design and phonon engineering in STE performance and provide guidance for next-generation ultrafast THz spintronic devices.

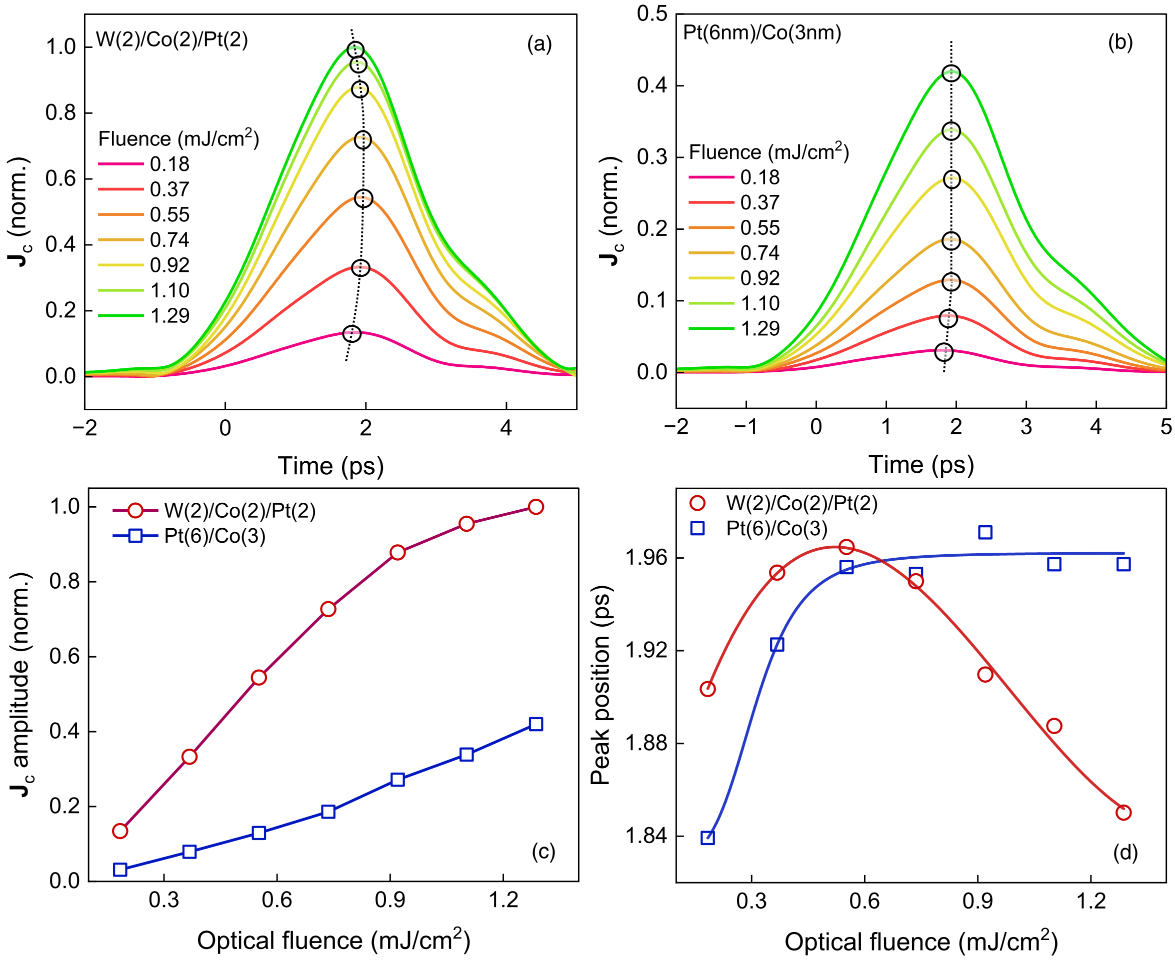

Fig. 4. Extracted charge currents ($\mathbf{J}_c$) at various optical fluences for (a) the trilayer and (b) the bilayer. (c) The extracted amplitudes and (d) peak positions of the $\mathbf{J}_c$ extracted for both STEs, respectively. The numbers in parentheses indicate the thickness in nm.

Acknowledgments This work was supported by the National Research Foundation of Korea (NRF) grant funded by the Korea government (MSIT)(RS-2024-00454395), and by the Pukyong National University Industry-university Cooperation Research Fund in 2023(202312120001). Additional support was provided by the Gwangju Institute of Science and Technology (GIST) research fund (Future-leading Specialized Research Project, 2025).

1) K. Lee, D. K. Lee, D. Yang, R. Mishra, D. J. Kim, S. Liu, Q. Xiong, S. K. Kim, K. J. Lee, and H. Yang, Nat. Nanotechnol. **16**, 1337 (2021).
2) J. Y. Bigot and M. Vomir, Ann. Phys. **525**, 2 (2013).
3) J. Walowski and M. Münzenberg, J. Appl. Phys. **120**, 140901 (2016).
4) M. Battiato, K. Carva, and P. M. Oppeneer, Phys. Rev. Lett. **105**, 027203 (2010).
5) E. Beaurepaire, J. Merle, A. Daunois, and J. Bigot, Phys. Rev. Lett. **76**, 4250 (1996).
6) J. Y. Bigot, M. Vomir, and E. Beaurepaire, Nat. Phys. **5**, 515 (2009).
7) X. Wang et al., Adv. Mater. **30**, 1802356 (2018).
8) T. Kampfrath et al., Nat. Nanotechnol. **8**, 256 (2013).
9) E. T. Papaioannou and R. Beigang, Nanophotonics **10**, 1243 (2021).
10) Z. Feng, H. S. Qiu, D. H. Wang, C. H. Zhang, S. Sun, B. B. Jin, and W. Tan, J. Appl. Phys. **129**, 010901 (2021).
11) L. Cheng, Z. Q. Li, D. M. Zhao, and E. E. M. Chia, APL Mater. **9**, 070902 (2021).
12) T. S. Seifert, L. Cheng, Z. X. Wei, T. Kampfrath, and J. B. Qi, Appl. Phys. Lett. **120**, 180401 (2022).
13) Y. Wu, M. Elyasi, X. Qiu, M. Chen, Y. Liu, L. Ke, and H. Yang, Adv. Mater. **29**, 1603031 (2017).
14) T. Seifert et al., Nat. Photon. **10**, 483 (2016).
15) R. Rouzegar et al., Phys. Rev. Appl. **19**, 034018 (2023).
16) G. Gandubert, J. E. Nkeck, X. Ropagnol, D. Morris, and F. Blanchard, Appl. Phys. Express **17**, 083001 (2024).
17) K. Lee et al., ACS Nano **13**, 9587 (2019).
18) A. Leitenstorfer, S. Hunsche, J. Shah, M. C. Nuss, and W. H. Knox, Appl. Phys. Lett. **74**, 1516 (1999).
19) A. M. Ulatowski, L. M. Herz, and M. B. Johnston, J. Infrared Milli. Terahz Waves **41**, 1431 (2020).
20) S. S. Mishra, J. Lourembam, D. J. X. Lin, and R. Singh, Nat. Commun. **15**, 4568 (2024).
21) M. Mo et al., Sci. Adv. **10**, eadk9051 (2024).